



Insight Into the Preferential N-Binding versus O-Binding of Nitrosoarenes to Ferrous and Ferric Heme Centers

| | |
|-------------------------------|--|
| Journal: | <i>Dalton Transactions</i> |
| Manuscript ID | DT-ART-10-2020-003604.R2 |
| Article Type: | Paper |
| Date Submitted by the Author: | 06-Feb-2021 |
| Complete List of Authors: | <p>Abucayon, Erwin; University of Oklahoma, Dept of Chemistry and Biochemistry Chu, Jia-Min; Stevens Insitute of Technology, Chemistry and Chemical Biology Ayala, Megan; University of Oklahoma, Chemistry and Biochemistry Khade, Rahul; Stevens Institute of Technology, Chemistry and Chemical Biology Zhang, Yong; Stevens Insitute of Technology, Department of Chemistry and Chemical Biology Richter-Addo, G.; University of Oklahoma, Chemistry and Biochemistry</p> |
| | |

ARTICLE

Insight Into the Preferential *N*-Binding versus *O*-Binding of Nitrosoarenes to Ferrous and Ferric Heme Centers

Received 00th January 20xx,
Accepted 00th January 20xx

Erwin G. Abucayon,^a Jia-Min Chu,^b Megan Ayala,^a Rahul L. Khade,^b Yong Zhang,^{* b} and George B. Richter-Addo^{* a}

DOI: 10.1039/x0xx00000x

Abstract: Nitrosoarenes (ArNOs) are toxic metabolic intermediates that bind to heme proteins to inhibit their functions. Although much of their biological functions involve coordination to the Fe centers of hemes, the factors that determine *N*-binding or *O*-binding of these ArNOs have not been determined. We utilize X-ray crystallography and density functional theory (DFT) analyses of new representative ferrous and ferric ArNO compounds to provide the first theoretical insight into preferential *N*-binding versus *O*-binding of ArNOs to hemes. Our X-ray structural results favored *N*-binding of ArNO to ferrous heme centers, and *O*-binding to ferric hemes. Results of the DFT calculations rationalize this preferential binding on the basis of the energies of associated spin-states, and reveal that the dominant stabilization forces in the observed ferrous *N*-coordination and ferric *O*-coordination are $d\pi\text{-}p\pi^*$ and $d\sigma\text{-}p\pi^*$, respectively. Our results provide, for the first time, an explanation why *in situ* oxidation of the ferrous-ArNO compound to its ferric state results in the observed subsequent dissociation of the ligand.

Introduction

Nitrosoarenes and -alkanes ($R\text{-N=O}$; R = aryl, alkyl) are generated *in vivo* and *in vitro* from the reduction of nitroorganics (RNO_2) or from the oxidation of amine-containing (RNH_2) drugs. This class of compounds frequently displays biological activity as a result of interactions with metalloproteins.¹⁻⁵ The coordination chemistry of RNO compounds is fairly well established.⁶⁻⁸ For monomeric RNO ligands, their coordination to monometallic systems may occur through the N-atom, the O-atom, or through both atoms in a side-on *N,O*-binding fashion (Figure 1).

Interactions of RNO compounds with heme proteins are particularly relevant to their bioinorganic chemistry.^{7, 8} For example, in heme proteins containing exposed cysteine residues (e.g., human hemoglobin (Hb)), the RNO species may

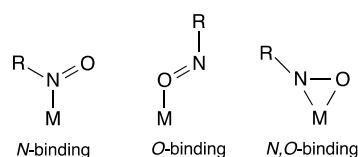


Figure 1. Binding modes of monomeric RNO ligands to monometallic centers.

interact directly with heme Fe and/or with the cysteine residues (e.g., β Cys93 in Hb) to alter their functions.^{9, 10} Importantly, the inhibition of heme enzymes such as cytochrome P450 after metabolic activation of amine-containing drugs to their nitroso derivatives has been known for decades.¹¹⁻¹³ Confirmation of RNO as an inhibitory ligand that can bind to heme Fe centers was first reported by Mansuy in 1977 for a synthetic heme model system,^{14, 15} with the heme model-RNO product displaying a similar UV-vis spectrum to that of the valence isoelectronic oxyferrous heme. Surprisingly, only a few heme protein-RNO derivatives of ferrous Hb, legHb, and myoglobin (Mb) have been characterized by X-ray crystallography,¹⁶⁻¹⁹ and the data to date reveal an *N*-binding mode of the RNO ligands to the ferrous heme centers.

A particularly interesting class of RNO compounds are those that contain *para*-amino functionalities, namely the *p*-nitrosodialkylanilines (Figure 2). Both NODMA and NODEA are

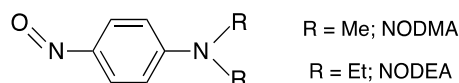


Figure 2. The nitrosoarenes NODMA and NODEA.

^a Dr. Erwin G. Abucayon, Megan Ayala, Dr. George B. Richter-Addo
Department of Chemistry and Biochemistry
University of Oklahoma
101 Stephenson Parkway
Norman, OK 73019
E-mail: grichteraddo@ou.edu

^b Jia-Min Chu, Dr. Rahul L. Khade, Dr. Yong Zhang
Department of Chemistry and Chemical Biology
Stevens Institute of Technology
Castle Point on Hudson
Hoboken, NJ 07030
E-mail: yong.zhang@stevens.edu

† Footnotes relating to the title and/or authors should appear here.
Electronic Supplementary Information (ESI) available: [details of any supplementary information available should be included here]. See DOI: 10.1039/x0xx00000x

toxic, mutagenic, and exhibit bactericidal effects.²⁰ NODMA-dependent alcohol dehydrogenase enzymes are also known.²¹ As with other nitrosoarenes, NODMA is known to interact with Hb to inhibit its oxygen transport function resulting in difficulty breathing, and can induce the onset of methemoglobinemia.^{22–24} Coordination and bioinorganic compounds of NODMA and NODEA have been reported, with both *N*- and *O*-binding to the transition metals established by X-ray crystallography.^{25–30}

A useful historical predictor of the mode of binding of nitrosoarenes derives from consideration of the Hard-Soft Acid-Base concept. In a seminal paper by Pearson on the topic,³¹ metal cations such as Fe³⁺ and Co³⁺ are classified as "hard acids" that have favorable interactions with hard bases such as *O*-donors, whereas Pt²⁺, Ag⁺, Cu⁺ are considered "soft acids" that favor interaction with soft bases such as *S*-donors. Metal cations such as Fe²⁺, Co²⁺, and Zn²⁺ are considered "borderline". Indeed, this predictor, in many cases, has helped rationalize binding modes of ligands in several coordination complexes, especially those of biological relevance. The Hard-Soft Acid-Base concept, despite being useful in many cases, has not been sufficient in explaining some experimental observations of preferred binding modes, especially when it comes to heme model complexes. For example, the X-ray crystal structure of the model heme complex [(TPP)Co(NODMA)₂]SbF₆ (TPP = tetraphenylporphyrinato dianion) reveals an experimental *N*-binding of the ligand to the hard Co³⁺ metal center,²⁸ in preference to the predicted *O*-binding mode. Some flexibility was also observed when soft cations such as Cu⁺ interact with nitrosoarenes to result in complexes displaying either the *N*-binding or *O*-binding modes.^{29, 32, 33} Further, an *O*-binding mode of a nitrosoarene was established in a complex of the borderline Zn²⁺ cation.³⁴ This situation is complicated further upon consideration of the fact that nitrosoarenes are themselves redox active that can serve as π -acid ligands towards metal centers.^{8, 35, 36}

To date, *N*-binding of RNO ligands to ferrous heme proteins and models appears to be the favored binding mode based on the experimental data. Oxidation of the ferrous heme–RNO complexes generally results in spectral changes that are accompanied by the loss of the RNO ligand or its modified form (Figure 3). In particular, addition of ferricyanide as an oxidant to solutions of RNO-adducts of ferrous Hb,^{37, 38} Mb,³⁷ cyt P450,^{13, 39–41} NO synthase,⁴² microperoxidase 8,^{43, 44} and prostaglandin H synthase⁴⁵ all results in the dissociation of the respective RNO groups from the ferric centers. In some cases, ferric intermediates "Fe(III)-RNO" (middle of Figure 3) with presumed weak interactions between the ferric centers and RNO ligands were observed,^{42, 43, 45} although the exact nature

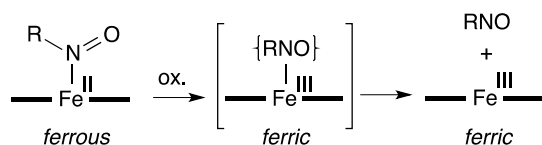


Figure 3. Oxidation of ferrous heme-RNO compounds.

of RNO binding to the ferric centers was not established.

We previously reported our preliminary results of nitrosoarene *N*-binding to the ferrous center of (TPP)Fe(PhNO)₂, and *O*-binding to the ferric center of [(TPP)Fe(NODEA)₂]⁺.²⁷ However, issues with extensive disorder in the crystal structure of the latter *O*-bound derivative, and the fact that two different nitrosoarenes were used for these two derivatives, prevented a reliable comparison of their structural properties to assess the effects of *N*-binding versus *O*-binding on their relative stabilities. In this paper, we report the investigation of preferential binding modes of the NODMA and NODEA ligands to ferrous and ferric porphyrin centers. Importantly, we employ X-ray crystallography to provide the first direct comparison regarding the geometrical binding preferences as a function of Fe oxidation state in heme models that are relevant to some biological systems. In addition, our Density Functional Theory (DFT) calculations offer the first theoretical support of such a differential coordination mode change due to the Fe oxidation state with data from energies and optimized structures. Our DFT results also revealed previously unknown electronic insights of charges and molecular orbital features into the preferred stabilities of the experimentally observed coordination modes. These results help provide an understanding of the biological binding motifs of RNO compounds in ferrous and ferric heme proteins and their model systems.

Results and Discussion

As this study focuses on the structural and electronic consequences of nitrosoarene binding to Fe^{II} and Fe^{III} heme centers, it is informative to first consider the properties of the free ligands. The crystal structures of NODMA^{46, 47} and NODEA⁴⁸ have been reported. Both structures suffer from disorder in their –CNO fragments, but the overall geometrical data sufficiently define a substantial contribution of the zwitterionic quinoidal structure shown on the right of Figure 4.

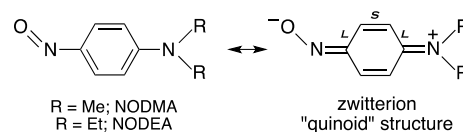


Figure 4. Zwitterion contributions to NODMA and NODEA.

Consistent with the significant zwitterionic contribution are (i) the planarity of the ONC₆H₄NR₂ core, (ii) the observed long (*L*) and short (*S*) bond-length alteration within the aryl –C₆H₄– fragment, and (iii) the larger (O)NCC angles *cis* to the nitroso O than *trans* to O (by ~10–15°) attributed to intramolecular repulsive interactions involving the nitroso O-atom. This zwitterionic contribution appears to correlate with the difficulty of assigning the vibrational stretching frequency of the NO bond (ν_{NO}). Unlike most nitrosoalkanes and nitrosoarenes where ν_{NO} 's have been assigned with reasonable confidence,^{7, 49} the ν_{NO} 's of NODMA and NODEA (both free and liganded) have historically been the subject of much

controversy, as discussed by Gowenlock, Cameron, and Lüttke.⁵⁰⁻⁵³ Contributing to this difficulty in ν_{NO} assignment is the extensive vibrational coupling between ν_{NO} and ν_{CC} and ν_{CH} . This is evidenced by the number of IR bands that shift in response to ^{15}N -nitroso and ^{18}O -nitroso isotopic substitution for both NODMA (Figure 5, top) and NODEA (Figure 5, bottom); a dynamic visual of this vibrational coupling is shown in the Figure S5 movie file in the SI. Perhaps the most reliable reported assignment of ν_{NO} of NODMA to date is that provided in the Ph.D. dissertation of Knieriem⁵⁴ that documents a similar observation of multiple ^{15}N -isotope sensitive band shifts, and assigns a ν_{NO} value of 1363 cm^{-1} based on both ^{15}NO and ^2H isotope substitutions.

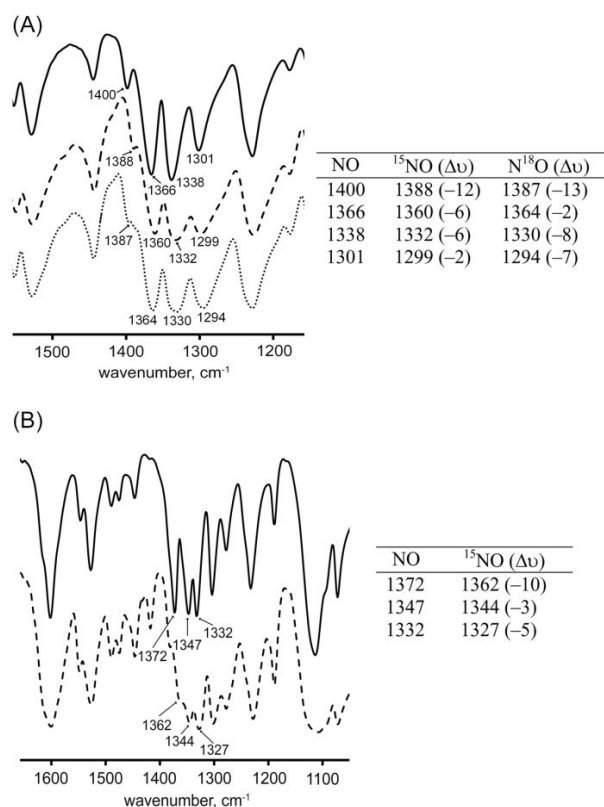


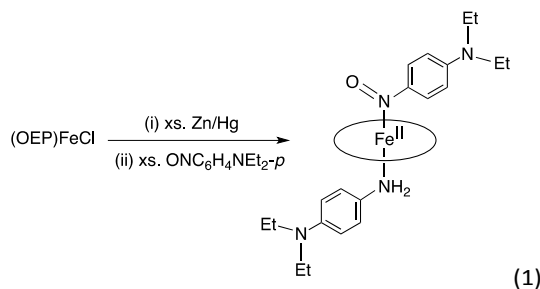
Figure 5. Truncated FTIR spectra of NODMA and NODEA (KBr pellets) and their ^{15}N -nitroso (broken line trace) and ^{18}O -nitroso (dotted line trace) isotope-substituted derivatives. The major isotope-sensitive bands in these truncated regions are shown in the respective boxes. See Figures S1-S4 in the SI for additional characterization data.

Given the historical complexity of ν_{NO} assignment in NODMA and NODEA in both the free ligands and their metal complexes, it is not surprising that the unambiguous determinations of *N*- vs. *O*-binding modes of NODMA/NODEA to metal centers have been through the use of X-ray crystallography. For example, a proposed *O*-binding mode of NODMA to a cobalt center based on IR spectroscopy^{55, 56} was revised to an *N*-binding mode based on X-ray crystallography.²⁵ Indeed, the IR spectra of the complexes prepared in this current work (Experimental Section, and Figures S6 and S8-S10 in the SI) reveal several ^{15}N -nitroso and ^{18}O -nitroso isotope sensitive bands, making it difficult to

unambiguously assign the ν_{NO} vibrations in these compounds. Consequently, obtaining crystal structures of both the ferrous and ferric derivatives of NODMA and NODEA became an absolute requirement for our study in order to assign the binding modes with confidence.

The Ferrous Systems

Reaction of NODEA with in situ-generated ferrous d^6 (OEP)Fe^{II}, in a manner similar to that used for the preparation of (TPP)Fe(PhNO)₂,²⁷ resulted in the formation of the *mono*-nitrosoarene adduct (OEP)Fe(NODEA)(NH₂C₆H₄NEt₂-*p*) (eq 1).



The complex was isolated in good yield and is air-stable as a solid for several days. To date, we have been unable to obtain suitable crystals of the expected *bis*-ArNO (OEP)Fe(NODEA)₂ derivative. The six-coordinate *mono*-NODEA derivative was likely obtained due to the serendipitous in situ Zn-reduction of the NODEA reagent present in excess in the reaction mixture. We note that the chemical reduction of nitrosoarenes such as NODMA (e.g., by Zn or Fe, with proton sources) to their amines are well-known.⁵⁷

The molecular structure of (OEP)Fe(NODEA)(NH₂C₆H₄NEt₂-*p*) was identified by X-ray crystallography and is shown in Figure 6; selected bond lengths and angles for the structures obtained in this work are collected in Table 1. The axial N/O atoms in the crystal structure of (OEP)Fe(NODEA)-(NH₂C₆H₄NEt₂-*p*) exhibit a 90:10 positional disorder across the porphyrin plane (Figure S7). The Fe–N(por) bond lengths of 1.99–2.01 Å in (OEP)Fe(NODEA)(NH₂C₆H₄NEt₂-*p*) are consistent with those expected for ferrous d^6 low-spin hemes.⁵⁸ The axial Fe–N(O) bond length of 1.827(2) Å is shorter than that for the *trans* Fe–NH₂Ar bond length of 2.100(2) Å, with the latter being close to the 2.028(2)–2.043(3) Å bond lengths observed in the bis primary amine complexes (TPP)Fe(NH₂R)₂ (R = alkyl).⁵⁹ The slight lengthening of this Fe–NH₂Ar bond in (OEP)Fe(NODEA)(NH₂C₆H₄NEt₂-*p*) is likely due to the presence of the *trans* π -acceptor ArNO moiety. Consistent with this latter feature is the slight apical displacement of 0.13 Å of the Fe atom from the 24-atom porphyrin plane towards the ArNO ligand. In this structure, the NO group is oriented in a position that essentially bisects adjacent porphyrin N atoms.

There are several interesting structural features of the bound NODEA ligand in the crystal structure of (OEP)Fe(NODEA)(NH₂C₆H₄NEt₂-*p*). First, the O1–N7–C47–C48 torsion angle involving the nitroso group of the NODEA ligand

is 58.2(4)°, and this large deviation from the planarity substantially disrupts the overlap of the NO and aryl π systems

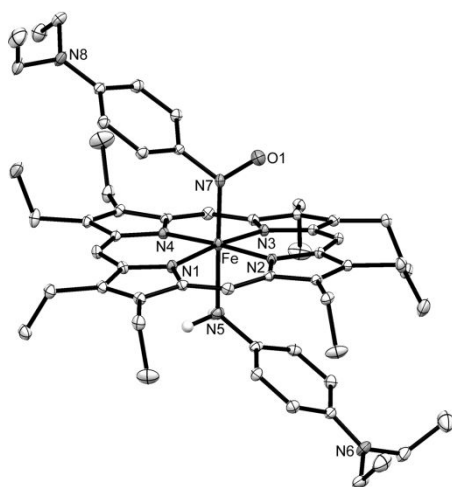


Figure 6. The molecular structure of (OEP)Fe(NODEA)(NH₂C₆H₄NEt₂-*p*) with thermal ellipsoids drawn at 35%. Only the major axially NO/NH₂-disordered (~90%) component is shown (see Figure S7).

observed in the free nitrosoarene.⁶⁰ Second, the (O)NCC bond angles associated with the ON–aryl link are similar for N7–C47–C48 (at 119.0(2)°) and N7–C47–C52 (at 121.2(2)°), with ~2° difference being much smaller than the 10–12° observed in the free ligand. Third, both the ON–C and (aryl)C–NEt₂ bond lengths are longer than those observed in the free ligand that has significant quinoidal character. Fourth, the aryl C–C bond lengths do not show the substantial alternating long-short-long trend observed in the free ligand (Table 1; c.f. Figure 4). We note that *N*-binding of NODEA/NODMA in metal derivatives does not necessarily result in such deviations from the quinoid structure of the free ligand,³⁰ and a twist angle of only ~4° from planarity was observed in an *N*-bound Co–NODMA complex.²⁵

We had anticipated that the observed significant deviation from planarity and quinoidal character of the NODEA ligand in (OEP)Fe(NODEA)(NH₂C₆H₄NEt₂-*p*) structure, in effect making the NODEA more of a "normal" ArNO ligand, would have allowed us to estimate the ν_{NO} in this complex. For example, Zhang and coworkers have used experimental IR data and detailed computational methods to establish an inverse correlation of $d(\text{N–O})$ with ν_{NO} in a series of heme–RNO/ArNO complexes.⁴⁹ Using their inverse correlation as a predictive tool, the experimental N–O bond length of 1.281(3) Å in (OEP)Fe(NODEA)(NH₂C₆H₄NEt₂-*p*) should correspond to a ν_{NO} of ~1250 cm⁻¹. Indeed, the IR spectrum of (OEP)Fe(NODEA)(NH₂C₆H₄NEt₂-*p*) reveals an ¹⁵N-nitroso isotope sensitive band at 1230 cm⁻¹ (Figure S6). However, we are hesitant to assign this band to an isolated vibration, as extensive vibrational coupling within NODMA/NODEA results in multiple bands being ¹⁵N- and ¹⁸O-isotope sensitive as described above (Figure 5).

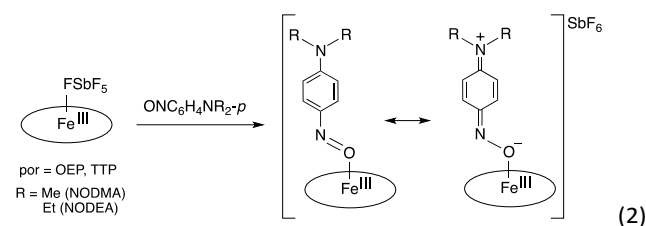
Table 1. Selected bond lengths (Å) and angles (°) for the structurally characterized ferrous and ferric compounds obtained in this work.

| | ferrous-OEP | ferric-OEP | ferric-TTP |
|-------------|---------------------------|-----------------------|-----------------------|
| Fe–N(O) | 1.827(2) ^[a] | - | - |
| Fe–O(N) | - | 1.9680(17) | 1.920(4) |
| N–O | 1.281(3) ^[a] | 1.318(2) | 1.334(5) |
| <i>a</i> | 1.463(3) ^[a] | 1.339(3) | 1.313(7) |
| <i>b/b'</i> | 1.388(3)/ 1.385(3) | 1.431(3)/ 1.412(3) | 1.425(8)/ 1.429(7) |
| <i>c/c'</i> | 1.379(3)/ 1.388(3) | 1.350(3)/ 1.355(4) | 1.347(8)/ 1.339(8) |
| <i>d/d'</i> | 1.407(3)/ 1.405(3) | 1.453(3)/ 1.444(4) | 1.452(8)/ 1.434(8) |
| <i>e</i> | 1.390(3) | 1.333(3) | 1.312(7) |
| ∠FeNO | 122.69(16) ^[a] | - | - |
| ∠FeON | - | 115.52(13) | 113.5(3) |
| ∠ONC | 110.59(18) ^[a] | 114.64(19) | 113.6(4) |

[a] Data for the major (~90%) NO/NH₂-disordered component.

The Ferric Systems

Reactions of the ferric porphyrin precursors (por)FeFSbF₅ (por = OEP, TTP) in CH₂Cl₂ with ~1.5 equiv of the nitrosoarenes (ArNO = NODMA and NODEA) result in the generation and subsequent isolation of the mono-nitrosoarene derivatives [(por)Fe(ArNO)]SbF₆ containing the uncoordinated anion. The use of <2 equiv of the nitrosoarene favors, in our hands, the isolation of the mono-nitrosoarene compounds that could be crystallized into well-resolved structures.



These five-coordinate [(por)Fe(ArNO)]SbF₆ compounds in CDCl₃ solvent displayed magnetic moments, determined by the Evans' method,⁶¹ of 4.8–4.9 BM suggesting admixed-spin systems of $S = 3/2$ and $5/2$ in solution.

The crystal structures of the cations of the ferric derivatives [(OEP)Fe(NODEA)]SbF₆ and [(TTP)Fe(NODMA)]SbF₆ are displayed in Figure 7. The most important feature of these structures is the determination of the *O*-binding mode of the nitrosoarene ligands to the ferric centers. The structure of the [(OEP)Fe(NODEA)]⁺ cation was ordered except for one of ethyl C-atoms of the terminal NEt₂ group. The Fe–N(por) bond lengths of 2.0284(18)–2.0529(18), the axial Fe–O length of 1.9680(17) Å, and the apical displacement of the Fe atom by +0.40 Å from the 24-atom mean porphyrin plane towards the NODEA ligand are consistent with its admixed-spin state. The

axial Fe–O–N moiety is situated in a position that eclipses a porphyrin N-atom, with a (por)N2–Fe–O–N(NODEA) torsion angle of $\sim 0.2^\circ$.

The crystal structure of the $[(\text{TTP})\text{Fe}(\text{NODMA})]^+$ cation is also ordered, with the exception of a methyl group of one of the porphyrin tolyl substituents. The geometrical data are also in the range of those determined for an admixed-spin system, with the NODMA ligand in this case oriented in a manner that essentially bisects a pair of adjacent porphyrin N-atoms, with a (por)N1–Fe–O–N5 torsion angle of $\sim 35^\circ$, and the Fe atom apically displaced by $+0.48 \text{ \AA}$ from the 24-atom mean porphyrin plane towards the axial ligand.

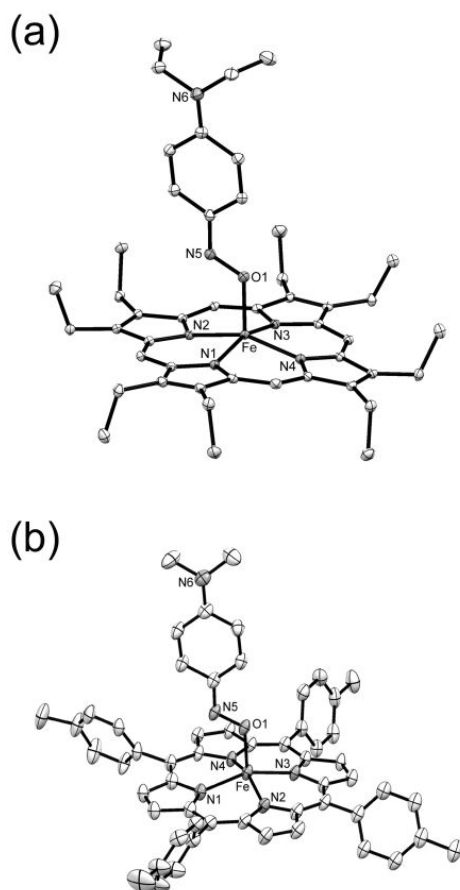


Figure 7. The crystal structures of the cations of (a) $[(\text{OEP})\text{Fe}(\text{NODEA})]\text{SbF}_6$, and (b) $[(\text{TTP})\text{Fe}(\text{NODMA})]\text{SbF}_6$, with thermal ellipsoids drawn at 35%.

Important differences are evident when comparing the geometrical parameters of the nitrosoarene ligands in the *O*-bound ferric complexes with that in the *N*-bound ferrous system described earlier. We will focus on the crystal structures of the ferrous and ferric OEP/NODEA pair, namely the *N*-bound $(\text{OEP})\text{Fe}^{\text{II}}(\text{NODEA})(\text{NH}_2\text{C}_6\text{H}_4\text{NEt}_2)$ versus the *O*-bound $[(\text{OEP})\text{Fe}^{\text{III}}(\text{NODEA})]^+$. The nitroso N–O bond length of $1.318(2) \text{ \AA}$ in the ferric *O*-bound complex is longer than the related distance of $1.281(3) \text{ \AA}$ in the ferrous *N*-bound derivative. Consistent with this is also the shorter (O)N–C bond length of $1.339(3) \text{ \AA}$ in the ferric complex compared with $1.463(3) \text{ \AA}$ in the ferrous case. Of particular note is the essential planarity of the $\text{ONC}_6\text{H}_4\text{N}$ -moiety in the ferric *O*-

bound complex with an O1–N5–C37–C38 torsion angle of $-0.6(3)^\circ$, and the larger N5–C37–C38 angle ($125.1(2)^\circ$; *cis* to nitroso-O) compared with the N5–C37–C42 angle ($116.0(2)^\circ$; *trans* to nitroso-O). In addition, the aryl C–C bonds in the *O*-bonded ferric system show the alternating long-short-long bond lengths similar to that observed in the free ligand (e.g., right of Figure 4).

Similar geometrical parameters are extant in the crystal structure of the ferric $[(\text{TTP})\text{Fe}(\text{NODMA})]^+$ derivative (Table 1). As with the ferrous-NODEA system, we are unable to determine a reliable assignment of ν_{NO} in these ferric derivatives due to extensive vibrational coupling even with ^{15}N -nitroso isotopic substitution (Figures S8 and S9 in the SI).

Computational Insight into the Preferential *N*- versus *O*-Binding of the Nitrosoarenes

In order to understand the electronic reasons for the preferential binding modes in the experimentally determined structures of the ArNO liganded ferrous and ferric hemes, we performed a quantum chemical investigation of model systems using ωB97XD , a recently developed hybrid Hartree-Fock and DFT method with dispersion correction. We have found this method to yield accurate predictions of various experimental spectroscopic properties, structural features, and reactivity results of iron porphyrin complexes.^{62–68} We focused on the electronic structures of the bis-ArNO and mono-ArNO liganded systems with no other axial ligands, to exclude possible secondary electronic effects of other *trans* ligands. Using the parent unsubstituted porphine macrocycle, we calculated the optimized geometries for both the *N*-binding mode for the ferrous ($\text{Fe}^{\text{II}}\text{-N}$) system (left panel of Figure 8) and *O*-binding mode for the ferric ($\text{Fe}^{\text{III}}\text{-O}$) mono-NODMA system, as well as the alternate but not observed $\text{Fe}^{\text{II}}\text{-O}$ and $\text{Fe}^{\text{III}}\text{-N}$ systems (right panel of Figure 8).

The geometry optimizations and energy calculations yielded results consistent with experiment. The optimized structure of the ferrous $\text{Fe}^{\text{II}}\text{-N}$ mode showed that the ground state is a singlet ($S = 0$), with the triplet and quintet states being $>10 \text{ kcal/mol}$ higher in Gibbs free energy that are accompanied by the dissociation of one or both ligands. This singlet ground state agrees with the experimental data for ferrous $(\text{por})\text{Fe}(\text{ArNO})_2$ ²⁷ and $(\text{por})\text{Fe}(\text{ArNO})\text{L}$ compounds,^{15, 60} and is also consistent with the fact that six-coordination in ferrous porphyrins is generally associated with the low-spin state.^{69, 70}

The calculations also showed that the ground state of the experimentally observed ferric $\text{Fe}^{\text{III}}\text{-O}$ mode is an admixed $S = 3/2$ and $S = 5/2$ spin state, as these two spin states are very close in energy; the energy (ΔG) of the high-spin state is only 2.22 kcal/mol higher than that of the intermediate-spin state (Table 2). This agrees with the experimental magnetic moment data in solution determined by the Evans method (Experimental Section). In contrast, the low-spin state ($S = 1/2$;

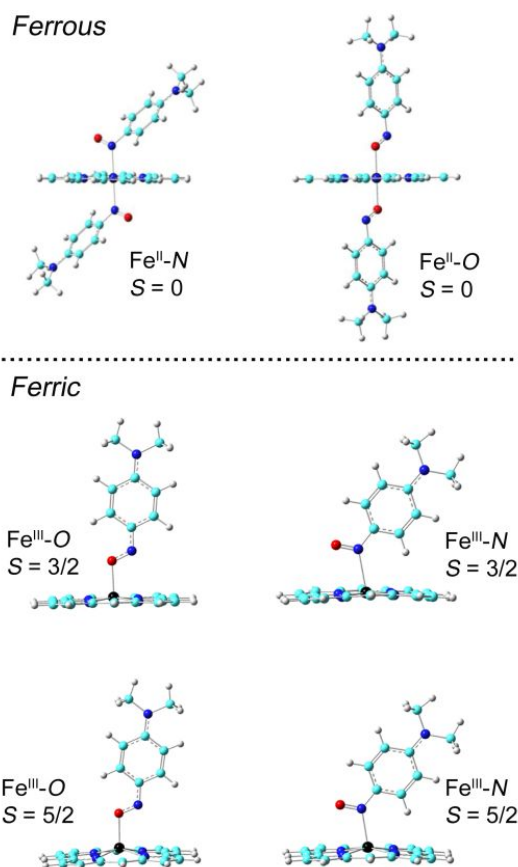


Figure 8. Optimized structures of the $\text{Fe}^{\text{II}}\text{-N}$ and $\text{Fe}^{\text{II}}\text{-O}$ (left panel) and alternate coordination geometries (right panel) of NODMA-coordinated ferrous and ferric porphyrins (atom colors: N-blue, O-red, C-cyan, H-grey, Fe-black).

Table 2. Relative Energy Results (in kcal/mol) of Iron Porphyrins with Favorable Spin States (S)

| Mode | S | ΔE | ΔE_{ZPE} | ΔH | ΔG |
|-----------------------------------|-----|------------|-------------------------|------------|------------|
| $\text{Fe}^{\text{II}}\text{-N}$ | 0 | 0.00 | 0.00 | 0.00 | 0.00 |
| $\text{Fe}^{\text{II}}\text{-O}$ | 0 | 11.65 | 10.59 | 11.08 | 8.22 |
| $\text{Fe}^{\text{III}}\text{-O}$ | 3/2 | 0.00 | 0.00 | 0.00 | 0.00 |
| | 5/2 | 5.77 | 3.31 | 3.82 | 2.22 |
| $\text{Fe}^{\text{III}}\text{-N}$ | 5/2 | 4.30 | 2.23 | 2.03 | 4.26 |
| | 3/2 | 6.44 | 5.29 | 5.38 | 5.99 |

not shown) is significantly higher in energy than the high-spin state by 6.52 kcal/mol. The spin density data in these ferric $\text{Fe}^{\text{III}}\text{-O}$ systems (Table 3) show that for the $S = 3/2$ spin state, the Fe center holds most of the spin density (2.836 e) with only 0.044 e located on the porphine macrocycle. In contrast, for the $S = 5/2$ spin state, the spin density is more generally distributed between the Fe center (3.729 e) and the porphine (1.221 e). This difference in spin density distribution is not unlike those observed in related $S = 5/2$ and $S = 3/2$ iron porphyrins.⁷¹

Table 3. Spin Densities (in e units) of the Ferric Porphyrins with Favorable Spin States

| System | S | $\rho_{\alpha\beta}^{\text{Fe}}$ | $\rho_{\alpha\beta}^{\text{Por}}$ | $\rho_{\alpha\beta}^{\text{L[a]}}$ |
|-----------------------------------|-----|----------------------------------|-----------------------------------|------------------------------------|
| $\text{Fe}^{\text{III}}\text{-O}$ | 3/2 | 2.836 | 0.044 | 0.120 |
| | 5/2 | 3.729 | 1.221 | 0.050 |
| $\text{Fe}^{\text{III}}\text{-N}$ | 3/2 | 2.023 | 0.961 | 0.004 |
| | 5/2 | 3.765 | 1.225 | 0.001 |

[a] L is the axial ligand.

Importantly, the calculated geometries, especially those involving the key bond lengths and angles involving the coordinated $\text{ONC}_6\text{H}_4\text{NR}_2\text{-}p$ ligands (Table 4), match very well with the experimentally determined structures, with a mean percentage error of 3%.

The energies (ΔG) of the alternate, but not experimentally observed, binding modes for the ArNO ligands (right panel of Figure 8, and Table 2) were also probed computationally using the favorable and experimentally observed spin states. For the ferrous system, the alternate $\text{Fe}^{\text{II}}\text{-O}$ binding mode is higher in energy than the experimentally observed $\text{Fe}^{\text{II}}\text{-N}$ binding mode by 8.22 kcal/mol. For the ferric systems, the alternate $\text{Fe}^{\text{III}}\text{-N}$ binding mode is higher in energy than the experimentally observed $\text{Fe}^{\text{III}}\text{-O}$ binding mode by an average of $\sim 4\text{-}6$ kcal/mol. These computational results clearly reveal that the experimentally observed ArNO coordination modes originate from the different relative stabilities of the N - and O -binding forms of the molecular ferrous and ferric systems, and are not artifacts resulting from crystal packing effects.

To help understand the origin of the observed different stabilities associated with the ferrous and ferric porphyrins, we first look into their geometries. As seen from Figure 8, regardless of iron oxidation state, the N - and O -coordinated ligands are tilted with respect to the porphyrin planes. However, there is an interesting trend when comparing the experimental structures of the ferrous N -coordinated and ferric O -coordinated forms: the Fe–ON bond length is longer than the Fe–NO, and the O -coordination is associated with a longer N–O bond length, a shorter (O)N–C bond length, larger phenyl C–C bond length variations (the difference between average of (N)C–C and the "internal" C–C bonds), as well as shorter C–N(Et₂) bond lengths, compared to the N -coordination. These structural changes point to a resonance structure difference as shown in Figure 4, i.e., the O -coordination prefers the right zwitterionic resonance structure, while the N -coordination favors the left neutral resonance structure, consistent with the X-ray structural data shown in Table 1.

This feature of zwitterionic contribution is further supported by the charge analysis results as shown in Table 5. Compared to the almost neutral NO moiety (-0.074 e) in the N -coordinated ferrous porphyrin $\text{Fe}^{\text{II}}\text{-N}$, the NO fragment is significantly more anionic with a -0.359 e charge in the O -coordinated ferric porphyrin $\text{Fe}^{\text{III}}\text{-O}$, averaged for the $S = 3/2$ and $5/2$ admixed states. In general, because O is more

Table 4. Selected Geometric Parameters of Iron Porphyrins with Favorable Spin States (Units: Å and ° for bond length and bond angles respectively)

| Mode | S | Fe–N _{por} ^[a] | Fe–N/O ^[b] | N–O | <i>a</i> ^[c] | <i>b/d</i> ^[c] | <i>c</i> ^[c] | <i>e</i> | ∠FeNO/FeON | ∠ONC |
|---------------------------|----------------------|------------------------------------|-----------------------|-------|-------------------------|---------------------------|-------------------------|----------|------------|-------|
| Fe^{II}-N | Expt. ^[d] | 1.999 | 1.827 | 1.281 | 1.463 | 1.396 | 1.384 | 1.390 | 122.7 | 110.6 |
| | Calc. ^[e] | 0 | 2.020 | 2.032 | 1.210 | 1.421 | 1.405 | 1.381 | 119.0 | 114.1 |
| Fe^{II}-O | Calc. | 0 | 2.017 | 1.984 | 1.225 | 1.394 | 1.411 | 1.378 | 119.7 | 114.6 |
| Fe^{III}-O | Expt. ^[f] | | 2.060 | 1.921 | 1.334 | 1.312 | 1.435 | 1.343 | 113.4 | 113.6 |
| | Calc. | 3/2 | 1.988 | 2.073 | 1.256 | 1.348 | 1.427 | 1.365 | 114.3 | 116.1 |
| | | 5/2 | 2.105 | 2.087 | 1.255 | 1.354 | 1.425 | 1.366 | 112.7 | 116.1 |
| Fe^{III}-N | Calc. | 3/2 | 2.007 | 2.380 | 1.220 | 1.390 | 1.416 | 1.373 | 111.3 | 117.2 |
| | | 5/2 | 2.088 | 2.213 | 1.223 | 1.384 | 1.417 | 1.372 | 109.9 | 118.0 |

[a] averaged for four Fe–N_{por} bonds. [b] axial coordination to N or O. [c] average of aryl bond lengths as defined in Table 1. [d] (OEP)Fe(NODEA)(NH₂C₆H₄NEt₂-*p*) (major component). [e] for the bis-NODMA compound. [f] [(TTP)Fe^{III}(NODMA)]⁺.

electronegative than N, the *O*- and *N*-coordination may prefer the zwitterionic and neutral forms, respectively. It is interesting to note that, even for the ferrous systems, the change from *N*-coordination (**Fe^{II}-N**) to *O*-coordination (**Fe^{II}-O**) also results in a similar structural variation pattern of the nitrosoarene toward zwitterionic character (although quantitatively smaller): a shorter Fe–ON coordination bond, a longer N–O bond length, a shorter (O)N–C bond length, larger phenyl C–C bond length variations, and a shorter C–N(Me₂) bond length, as seen from Table 4, and a more anionic NO (Table 5). The same structural and charge variation pattern toward zwitterionic character also occurs in moving from *N*-coordination (**Fe^{III}-N**) to *O*-coordination (**Fe^{III}-O**) for the ferric porphyrins.

Table 5. Atomic Charges (in e units) of Iron Porphyrins with Favorable Spin States

| System | S | Q _{Fe} | Q _{por} | Q _{NO} |
|--|-----|-----------------|------------------|-----------------|
| Fe^{II}-N^[a] | 0 | 0.231 | −0.737 | −0.074 |
| Fe^{II}-O | 0 | 0.399 | −0.824 | −0.131 |
| Fe^{III}-O | 3/2 | 1.079 | −0.355 | −0.334 |
| | 5/2 | 1.111 | −0.299 | −0.384 |
| Fe^{III}-N | 3/2 | 0.776 | 0.064 | −0.277 |
| | 5/2 | 1.089 | −0.269 | −0.300 |

[a] Averaged for the same two ligands.

Due to the ferric center in **Fe^{III}-O** having a much higher positive charge than in the ferrous porphyrin **Fe^{II}-N** (~0.9 e, Table 5), it can be better stabilized by the more zwitterionic ligand form and thus favor the anionic *O*-coordination mode, while the more neutral ferrous center will favor the more neutral *N*-coordination mode. This is supported by the calculated energy trend that shows that *N*-coordination is more thermodynamically favored than *O*-coordination for ferrous porphyrins, while the opposite trend is observed for ferric porphyrins.

We then probed the electronic nature of the preferred *N*- and *O*-coordination modes for the ferrous and ferric porphyrins. The relevant MOs that involve significant interactions between Fe orbitals and the axial ArNO ligands in both the ferrous and ferric systems are shown in Figure 9. For ferrous **Fe^{II}-N** (Figure 9a), the π-type bonding between the Fe

*d*_π orbitals (including both *d*_{xz} and *d*_{yz}) and ligand *p*_{π*} orbitals can be clearly seen in the HOMO region (HOMO-4 and HOMO-5), while the σ-type bonding between the Fe *d*_{z2} orbital and the ligand is in the LUMO region (LUMO+9). This suggests dominant π-bonding interactions that stabilize the ferrous *N*-coordination mode.

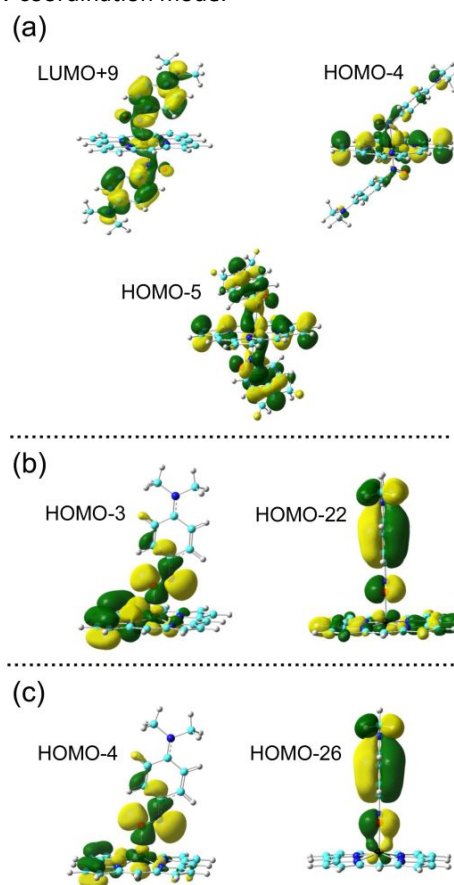


Figure 9. The MOs involving Fe and NO interactions for (a) the ferrous **Fe^{II}-N** complex (porphine)Fe(NODMA)₂, (b) the ferric **Fe^{III}-O** complex [(porphine)Fe-(NODMA)]⁺ with *S* = 3/2, and (c) the latter ferric **Fe^{III}-O** complex with *S* = 5/2. Contour values = ±0.02 au. The MO numbering is for the α spin.

In contrast, there are three significant differences that are evident for the MOs in the ferric **Fe^{III}-O** systems for both the *S* = 3/2 (Figure 9b) and *S* = 5/2 (Figure 9c) spin states.

First, the σ -type interaction between the Fe d_{z^2} orbital and the ArNO in-plane (i.e., ligand plane) π^* orbitals is now located in the HOMO region (HOMO-3). Second, unlike the two Fe d_{π} and ArNO π^* interactions that are present in the ferrous complex, there is only one major Fe d_{π} and ArNO π interaction in the case of ferric **Fe^{III}-O**, which involves the out-of-plane (i.e., perpendicular to the ligand plane) π orbital with antibonding (HOMO-22 in Figure 9b) and bonding (HOMO-26 in Figure 9c) interactions with the Fe d_{yz} orbital in the $S = 3/2$ and $S = 5/2$ spin states, respectively. Third, the σ -type bonding is more important than the π -type of bonding for ferric **Fe^{III}-O** system, due to the fact that the σ -type bonding is near the surface of HOMO region, while the π -type interaction is located in inner MOs as indicated by the relative MO numbering in Figure 9b-c. This kind of bonding helps stabilize the **Fe^{III}-O** σ interaction between the ferric center and the anionic *O*-coordination from the zwitterionic resonance contribution, as also noted above from the calculations of the structures and charges.

Conclusion

We have reported the preparation and crystal structural characterization of ferrous and ferric Fe–ArNO heme model compounds, and demonstrate that *N*-binding of the *para*-amino substituted ArNO ligand is favored for ferrous heme, and *O*-binding is favored for ferric heme. Examination of the geometrical features reveals that the quinoidal/zwitterionic character of the *para*-substituted ArNO ligand is prominent in the *O*-bound ferric system. Our results from DFT calculations on the *N*-binding and *O*-binding modes as a function of Fe oxidation and spin state are consistent with the experimentally observed preferential *N*- and *O*-binding modes in the ferrous and ferric systems, respectively.

Overall, these results provide the first theoretical comparisons of structural features, charges, and molecular orbital interactions due to Fe–N/O coordination in ArNO porphyrin complexes, and reveal that the dominant stabilization forces in the observed ferrous *N*-coordination and ferric *O*-coordination are $d_{\pi}-p\pi^*$ and $d_{\sigma}-p\pi^*$, respectively. These results support the experimentally observed *N*-coordination of RNO compounds to ferrous heme proteins and the subsequent dissociation of such ligands upon *in situ* oxidation to the ferric state,^{13, 37-44} due to the instability of *N*-coordination to ferric centers as revealed here.

Experimental Section

General: The reactions were performed anaerobically under an atmosphere of nitrogen unless otherwise noted. Air-sensitive samples and reagents were handled inside a glove box and all reactions were performed using standard Schlenk glassware. Solvents were dried using a Pure Solv 400-5-MD (Innovative Technology) solvent purification system, or distilled from appropriate drying agents under nitrogen. The free base porphyrin OEPH₂ (octaethylporphyrin) was purchased from Frontier Scientific, and TTPH₂ (tetratolylporphyrin) was synthesized by the Adler method.⁷² The metalloporphyrins (por)FeX (por = OEP, TTP; X

= Cl, SbF₆)⁷³⁻⁷⁵ and Zn/Hg⁷⁶ were prepared according to published procedures. Silver hexafluoroantimonate (AgSbF₆, 99%), *N,N*-diethyl-4-nitrosoaniline (*p*-Et₂NC₆H₄NO; NODEA, 97%), *N,N*-dimethyl-4-nitrosoaniline (*p*-Me₂NC₆H₄NO; NODMA, 97%), and Dowex 50WX2 were purchased from Sigma-Aldrich and were used as received. ¹⁸O-labeled water was purchased from Icon Isotopes. Na¹⁵NO₂ and chloroform-*d* (CDCl₃, 99.96%D) was purchased from Cambridge Isotopes; CDCl₃ was deaerated by three freeze-pump-thaw cycles and stored over molecular sieves. IR spectra were collected on a Bruker Tensor 27 FTIR spectrometer. ¹H NMR spectroscopy was performed using a 400 MHz Varian NMR spectrometer. UHPLC-MS measurements were performed on a Waters (Milford, MA) Acquity chromatography system coupled with a Waters G2-Si Ion Mobility Q-TOF mass spectrometer equipped with an electrospray ionization source operated in positive ion mode.

¹⁵N-labeled *p*-Me₂NC₆H₄¹⁵NO (¹⁵NODMA). The ¹⁵N-labeled derivative was prepared in a similar manner to that used for the preparation of the unlabeled analogue,⁷⁷ but with slight modifications. To a cold (ice-bath) stirred solution of dimethylaniline (0.51 g, 4.21 mmol) in conc. HCl (~2 mL) was added a solution of Na¹⁵NO₂ (0.32 g, 4.57 mmol; in ~1 mL of H₂O). The solution was stirred for 1 hr while cold (<8 °C), during which time the color turned yellow-orange with formation of a dark yellow precipitate. The precipitate was collected by vacuum filtration, washed with HCl:H₂O (1:1 v/v, 3 x 10 mL) followed by ethanol (3 x 10 mL), and subsequently dried under vacuum to give *p*-Me₂NC₆H₄¹⁵NO·HCl in ~60% crude yield. This salt was neutralized by addition of enough water to form a paste of the salt to which aq. NaOH (3 M) was added until the solution turned basic (as judged using pH paper) and the color changed to a bright green. The neutralized product was then extracted using benzene (3 x 10 mL), the extract then concentrated by slow evaporation (at ~80 °C), and the resulting solution was cooled to yield crystals of the *p*-Me₂NC₆H₄¹⁵NO (¹⁵NODMA) product which were isolated by filtration and air-dried overnight (78% isolated yield). IR (KBr; major ¹⁵N-isotope sensitive bands): 1388, 1360, 1332, and 1299 cm⁻¹. ¹H NMR (δ ppm, CDCl₃, 500 MHz): 7.90 (v br, 2H, aryl-*H*), 6.69 (br, 2H, aryl-*H*), 3.18 (s, 6H, -N(CH₃)₂) (Figure S1 in the SI). ESI-TOF MS: *m/z* 152.0833 (calcd. 152.0836) (Figure S2 (middle) in the SI).

¹⁵N-labeled *p*-Et₂NC₆H₄¹⁵NO (¹⁵NODEA). The diethyl analogue *p*-Et₂NC₆H₄¹⁵NO (¹⁵NODEA) was prepared similarly, but using Na₂CO₃ as the neutralization agent (60% isolated yield). IR (KBr; major ¹⁵N-isotope sensitive bands): 1362, 1344, and 1327 cm⁻¹. ¹H NMR (δ ppm, CDCl₃, 500 MHz): 8.70 (v br, 2H, aryl-*H*), 6.67 (br, 2H, aryl-*H*), 3.51 (q, *J*_{CH} 7 Hz, 4H, -N(CH₂CH₃)₂), 1.28 (t, *J*_{CH} 7 Hz, 6H, -N(CH₂CH₃)₂) (Figure S3 in the SI). ESI-TOF MS: *m/z* 180.1158 (calcd. 180.1143) (Figure S4 (bottom) in the SI).

¹⁸O-labeled *p*-Me₂NC₆H₄N¹⁸O (¹⁸O-NODMA). The ¹⁸O-labeled nitrite used for this reaction was prepared following a literature procedure⁷⁸ but with modifications due to our inability to obtain anhydrous HCl during the COVID-19 lab shutdown restrictions. To a solution of vacuum dried NaNO₂ (0.38 g, 5.51 mmol) in cold ¹⁸O-labeled water (H₂¹⁸O, ~1.5 mL, ice bath) was added Dowex 50WX2 (~0.50 g) and allowed to warm to room temperature and kept at this temperature for ~24 h. In a separate vial, a stirred solution of dimethylaniline (0.62 g, 5.12 mmol) in cold H₂¹⁸O (~1.5 mL, ice bath) was mixed with Dowex 50WX2 (~0.75 g), and to this mixture was slowly added the mixture of NaNO₂/Dowex 50WX2, and stirred for an additional ~30 min. The color of the combined reaction solution turned deep green during this period. The solution was decanted from the Dowex resin, and the product was extracted using benzene (2 x 10 mL). The benzene extract was dried with anhydrous K₂CO₃, and the product isolated by evaporation of the benzene at ~80 °C and air-dried overnight. The remaining mixture, after the benzene extraction step, was neutralized with NaOH (3 M) to recover more product. The total yield of the product, our hands, was low (~5%). IR (KBr; major ¹⁸O-isotope sensitive bands): 1387, 1364, 1330, and 1294 cm⁻¹. ESI-TOF MS: *m/z* 153.0917 (calcd. 153.0908); the ratio of ¹⁸O-labeled:unlabeled NODMA

was 2:1, indicating ~66% isotope incorporation (Figure S2 (bottom) in the SI).

(OEP)Fe(NODEA)(NH₂C₆H₄NEt₂-p). To a THF (10 mL) solution of (OEP)FeCl (25.0 mg, 0.040 mmol) was added excess Zn/Hg (48.2 mg, 0.74 mmol in Zn) and the mixture stirred for 1 h, during which time the pale purple solution changed to a bright red-purple. The supernatant solution was transferred by cannula into a separate Schlenk tube. To this air-sensitive solution was added NODEA (18.0 mg, 0.10 mmol, 2.5 equiv), and the reaction mixture was stirred for an additional 1 h. The THF was removed in vacuo, and the residue was washed with anhydrous *n*-hexane (3 x 10 mL). The resulting solid was redissolved in CH₂Cl₂ (~1.5 mL) and transferred to a separate vial, and the solution carefully layered with *n*-hexane (~3 mL). Slow evaporation of the solvent mixture to dryness inside a glove box resulted in a formation of thin plates that were isolated by handpicking and identified by X-ray crystallography as (OEP)Fe(NODEA)(NH₂C₆H₄NEt₂-p) in ~80% yield based on Fe. As with the compounds below, X-ray structural determinations from several crystals from the batch revealed the formation of only one crystalline product. An IR spectrum (KBr) of the crystals revealed several ¹⁵N-nitroso isotope sensitive bands as shown in Figure S6 in the SI.

[(OEP)Fe(NODEA)]SbF₆. To a CH₂Cl₂ (10 mL) solution of (OEP)FeSbF₅ (13.8 mg, 0.017 mmol) was added NODEA (1.9 mg, 0.023 mmol, ~1.4 equiv). The mixture was stirred for 2 h during which time the color of the solution slowly changed from light purple to red. The solution was concentrated to about half volume and the product was precipitated using *n*-hexane (~15 mL). The supernate was decanted and the solid was washed with *n*-hexane (3 x 10 mL) and subsequently dried in vacuo. The solid was redissolved in CH₂Cl₂ (~1.5 mL) and carefully layered with *n*-hexane (~3 mL) in a vial inside the glove box. Slow evaporation of this solution to dryness inside a glove box afforded block-shaped crystals that were isolated by handpicking and identified as [(OEP)Fe(NODEA)]SbF₆ (~63% isolated yield) by X-ray crystallography. An IR spectrum (KBr) of the crystals revealed several ¹⁵N-nitroso isotope sensitive bands as shown in Figure S8 in the SI. A spin-only magnetic moment of 4.91 BM was determined for the crystalline complex in CDCl₃ (25 °C) by the Evan's NMR method, which suggests an admixed-spin system of *S* = 3/2 and 5/2.^{79, 80}

[(TTP)Fe(NODMA)]SbF₆. To a CH₂Cl₂ (10 mL) solution of (TTP)FeSbF₅ (31.2 mg, 0.033 mmol) was added NODMA (7.5 mg, 0.050 mmol, ~1.5 equiv.). The mixture was stirred for 2 h during which time the color changed from orange-red to red. The solution was concentrated under reduced pressure, and the product was precipitated with *n*-hexane (15 mL). The supernate was decanted and the solid was washed with *n*-hexane (3 x 10 mL) and subsequently dried in vacuo. The solid was redissolved in CH₂Cl₂ (~2 mL), and the solution carefully layered with *n*-hexane (5 mL). Placing the mixture at -25 °C for ~1 d resulted in the formation of crystals which were isolated by decanting the supernate and drying the crystals using a flow of nitrogen gas. The crystals were identified as [(TTP)Fe(NODMA)]SbF₆ (82% yield) using X-ray crystallography. An IR spectrum (KBr) of the crystals revealed several ¹⁵N-nitroso isotope sensitive bands as shown in Figure S9 in the SI. A spin-only magnetic moment of 4.78 BM was determined for the crystalline complex in CDCl₃ (25 °C) by the Evan's NMR method, which suggests an admixed-spin system of *S* = 3/2 and 5/2.^{79, 80}

X-ray crystallography. Single-crystal X-ray diffraction data were collected using a D8 QUEST diffractometer with a Bruker Photon II CPAD area detector⁸¹ and an Incoatec 1 μs microfocus Mo K α radiation source (λ = 0.71073 Å), or with a Bruker APEX ccd area detector.^{82, 83} Diffraction data were collected from the samples at 100(2) K. The structures were solved by direct methods and using the SHELXTL system and refined by full-matrix least-squares methods on *F*².⁸⁴ Details of crystal data and structural refinement parameters are collected in Table S1 in the SI. CCDC 2011046-2011048 contain the supplementary crystallographic data. These data can be obtained free of charge via

www.ccdc.cam.ac.uk/data_request/cif, or by emailing data_request@ccdc.cam.ac.uk, or by contacting The Cambridge Crystallographic Data Centre, 12, Union Road, Cambridge CB2 1EZ, UK; fax: +44 1223 336033.

(i) (OEP)Fe(NODEA)(NH₂C₆H₄NEt₂-p). A red plate-shaped crystal of dimensions 0.040 x 0.156 x 0.173 mm was selected for structural analysis. Cell parameters were determined from a non-linear least squares fit of 9890 peaks in the range 2.19 < θ < 26.93°. A total of 72590 data were measured in the range 2.191 < θ < 27.366° using ϕ and ω oscillation frames. The data were corrected for absorption by the empirical method⁸⁵ giving minimum and maximum transmission factors of 0.942 and 0.986. The data were merged to form a set of 11216 independent data with R(int) = 0.0828 and a coverage of 99.9%. The monoclinic space group *P*2₁/*n* was determined by systematic absences and statistical tests and verified by subsequent refinement. Non-hydrogen atoms were refined with anisotropic displacement parameters. Hydrogen atom (bonded to carbon) positions were initially determined by geometry and refined by a riding model. The axial NO/NH₂ ligands in the structure were disordered. The occupancies of atoms N7, O1 and N5 refined to 0.901(4) and 0.099(4) for the unprimed and primed atoms, respectively. Restraints on the positional and displacement parameters of the disordered atoms were required. Hydrogen atom displacement parameters were set to 1.2 times (1.5 for methyl) the displacement parameters of the bonded atoms. A total of 611 parameters were refined against 51 restraints and 11216 data to give wR(*F*²) = 0.1064 and *S* = 1.027 for weights of $w = 1/[\sigma^2(F^2) + (0.0330 P)^2 + 3.5800 P]$, where $P = [F_o^2 + 2F_c^2]/3$. The final R(*F*) was 0.0468 for the 7946 observed, [$F > 4\sigma(F)$], data. The largest shift/s.u. was 0.001 in the final refinement cycle.

(ii) [(OEP)Fe(NODEA)]SbF₆·CH₂Cl₂. A purple block-shaped crystal of dimensions 0.080 x 0.240 x 0.420 mm was selected for structural analysis. Cell parameters were determined from a non-linear least squares fit of 9975 peaks in the range 2.26 < θ < 29.22°. A total of 55564 data were measured in the range 1.393 < θ < 29.784° using ϕ and ω oscillation frames. The data were corrected for absorption by the empirical method⁸⁵ giving minimum and maximum transmission factors of 0.3728 and 0.4324. The data were merged to form a set of 13621 independent data with R(int) = 0.0400 and a coverage of 100.0%. The triclinic space group *P*-1 was determined by systematic absences and statistical tests and verified by subsequent refinement. Non-hydrogen atoms were refined with anisotropic displacement parameters. Hydrogen atom (bonded to carbon) positions were initially determined by geometry and refined by a riding model. Hydrogen atom displacement parameters were set to 1.2 times (1.5 for methyl) the displacement parameters of the bonded atoms. The anion was disordered, with occupancies refining to 0.9687(5) and 0.0313(5) for the unprimed and primed atoms, respectively; restraints on the positional and displacement parameters of the disordered atoms were required. The displacement parameters of the two Sb atoms were constrained to be equal. The occupancies of the ligand NEt₂ atoms C45 and C46 were also disordered and refined to 0.867(5) and 0.133(5) for unprimed and primed atoms, respectively. A total of 654 parameters were refined against 624 restraints and 13621 data to give wR(*F*²) = 0.1056 and *S* = 1.005 for weights of $w = 1/[\sigma^2(F^2) + (0.0560 P)^2 + 1.6400 P]$, where $P = [F_o^2 + 2F_c^2]/3$. The final R(*F*) was 0.0417 for the 11034 observed, [$F > 4\sigma(F)$], data. The largest shift/s.u. was 0.002 in the final refinement cycle.

(iii) [(TTP)Fe(NODMA)]SbF₆. A purple plate-shaped crystal of dimensions 0.024 x 0.132 x 0.233 mm was selected for structural analysis. Cell parameters were determined from a non-linear least squares fit of 9853 peaks in the range 2.31 < θ < 24.73°. A total of 80385 data were measured in the range 2.310 < θ < 25.383° using ϕ and ω oscillation frames. The data were corrected for absorption by the semi-empirical from equivalents method⁸⁵ giving minimum and maximum transmission factors of 0.833 and 0.981. The data were merged to form a set of 10138 independent data with R(int) = 0.0842 and a coverage of 99.9%. The monoclinic space group *P*2₁/*c* was determined by systematic

absences and statistical tests and verified by subsequent refinement. Non-hydrogen atoms were refined with anisotropic displacement parameters. Hydrogen atom (bonded to carbon) positions were initially determined by geometry and refined by a riding model. Hydrogen atom displacement parameters were set to 1.2 times (1.5 for methyl) the displacement parameters of the bonded atoms. The anion and one of the methyl groups (of TTP) were disordered. The occupancies of the C48 atom refined to 0.50(6) and 0.50(6) for the unprimed and primed atoms, respectively. The occupancies of the anion refined to 0.872(5) and 0.128(5) for the unprimed and primed atoms, respectively. Restraints on the positional and displacement parameters were required. A CH₂Cl₂ solvent molecule was severely disordered and its effects on the intensity data were removed using the *Squeeze* algorithm.⁸⁶ A total of 708 parameters were refined against 1157 restraints and 10138 data to give $wR(F^2) = 0.1637$ and $S = 1.053$ for weights of $w = 1/[\sigma^2(F^2) + (0.0520 P)^2 + 20.7200 P]$, where $P = [F_o^2 + 2F_c^2]/3$. The final $R(F)$ was 0.0636 for the 7048 observed, $[F > 4\sigma(F)]$, data. The largest shift/s.u. was 0.000 in the final refinement cycle.

Computational methodology. All calculations were performed using Gaussian 16.⁸⁷ Full geometry optimizations using the unsubstituted porphine (por) macrocycle were conducted for all studied chemical systems, with subsequent frequency calculations to verify the nature of the corresponding stationary states on their potential energy surfaces and provide zero-point energy corrected electronic energies (E_{ZPE} 's), enthalpies (H's), and Gibbs free energies (G's) at room temperature in addition to electronic energies (E's). The used method includes the ω B97XD⁸⁸ functional with the basis set LanL2DZ⁸⁹ for Fe, 6-311++G(2d,2p) for first shell atoms (porphyrin N atoms and RNO's NO moiety), and 6-31G(d) for the rest of the atoms, which was the same for all systems, all bonding situations, and all spin states studied here. This functional enabled accurate predictions of various experimental geometric parameters, spectroscopic properties, and reactivities of iron porphyrin complexes⁶²⁻⁶⁸ and other transition metal complexes,⁹⁰ and this basis set also well reproduced many experimental properties of similar NO/HNO heme systems.⁹¹⁻⁹³ The atomic charges and spin densities reported here are from the Natural Population Analysis (NPA) and Mulliken schemes respectively, as implemented in Gaussian 16.⁸⁷

Acknowledgements

This material is based upon work supported by (while GBR-A was serving at) the U.S. National Science Foundation (NSF; CHE-1900181). Any opinion, findings, and conclusions or recommendations expressed in this material are those of the authors and do not necessarily reflect the views of the NSF. We are also grateful to the U.S. National Institutes of Health (GM085774 to Y.Z.) for funding this work, and to the NSF MRI program (CHE-1726630 to GBR-A) for funds to purchase the X-ray diffractometer. We thank Dr. Douglas R. Powell (OU) for the X-ray structural solution of [(OEP)Fe(NODEA)]SbF₆ and assistance with the re-refinement of the other structures. We also thank Jennifer Londono for technical assistance. GBR-A is especially grateful to Professor Armin de Meijere at the University of Göttingen for retrieving, with the assistance of BK's spouse, a hardcopy of the Ph.D. dissertation of Dr. Burkhard Knieriem (reference 54) and mailing it to Oklahoma during the COVID-19 pandemic.

Conflicts of interest

"There are no conflicts to declare".

Keywords: nitrosoarene • X-ray crystallography • DFT • iron • porphyrinoids

References:

- M. Kiese, *Arch. Exptl. Pathol. Pharmacol.*, 1959, **235**, 360-364.
- F. Jung, *Biochem. Z.*, 1940, **305**, 248-260. *Chem. Abs.* **235**:472.
- M. A. Belisario, R. Pecce, A. Garofalo, N. Sannolo and A. Malorni, *Toxicology*, 1996, **108**, 101-108.
- J. H. Harrison and D. J. Jollow, *J. Pharmacol. Exp. Ther.*, 1986, **238**, 1045-1054.
- M. Roldan, E. Perez-Reinado, F. Castillo and C. Moreno-Vivian, *FEMS Microbiol. Rev.*, 2008, **32**, 474-500.
- M. Cameron, B. G. Gowenlock and G. Vasapollo, *Chem. Soc. Rev.*, 1990, **19**, 355-379.
- J. Lee, L. Chen, A. H. West and G. B. Richter-Addo, *Chem. Rev.*, 2002, **102**, 1019-1065.
- N. Xu and G. B. Richter-Addo, *Prog. Inorg. Chem.*, 2014, **59**, 381-445.
- P. Eyer and M. Ascherl, *Biol. Chem. Hoppe-Seyler*, 1987, **368**, 285-294.
- P. Eyer and E. Lierheimer, *Xenobiotica*, 1980, **10**, 517-526.
- M. R. Franklin, *Chem.-Biol. Interact.*, 1976, **14**, 337-346.
- C. Bensoussan, M. Delaforge and D. Mansuy, *Biochem. Pharmacol.*, 1995, **49**, 591-602.
- D. Mansuy, P. Gans, J.-C. Chottard and J.-F. Bartoli, *Eur. J. Biochem.*, 1977, **76**, 607-615.
- D. Mansuy, P. Battioni, J. C. Chottard and M. Lange, *J. Am. Chem. Soc.*, 1977, **99**, 6441-6443.
- D. Mansuy, P. Battioni, J.-C. Chottard, C. Riche and A. Chiaroni, *J. Am. Chem. Soc.*, 1983, **105**, 455-463.
- J. Yi, G. Ye, L. M. Thomas and G. B. Richter-Addo, *Chem. Commun.*, 2013, **49**, 11179-11181.
- D. M. Copeland, A. H. West and G. B. Richter-Addo, *Proteins: Struct., Func., Genet.*, 2003, **53**, 182-192.
- S. M. Powell, L. M. Thomas and G. B. Richter-Addo, *J. Inorg. Biochem.*, 2020, **213**, 111262.
- I. P. Kuranova, A. V. Teplyakov, G. V. Obmolova, A. A. Voronova, A. N. Popov, D. M. Kheiker and E. G. Harutyunyan, *Bioorg. Khim.*, 1982, **8**, 1625-1636 (in Russian). *Chem. Abstr.* CA1698:48994.
- C. M. Goodall, C. M. Moore and O. B. Stephens, *Xenobiotica*, 1986, **16**, 587-593.
- T. Dausmann, A. Aivasidis and C. Wandrey, *Eur. J. Biochem.*, 1997, **248**, 889-896.
- O. Bodansky, *Pharmacol Rev*, 1951, **3**, 144-196.
- J. H. Harrison and D. J. Hollow, *Mol. Pharmacol.*, 1987, **32**, 423-431.
- T. E. Kearney, A. S. Manoguerra and J. V. Dunford, Jr., *West. J. Med.*, 1984, **140**, 282-286.
- D. B. Sams and R. J. Doedens, *Inorg. Chem.*, 1979, **18**, 153-156.
- S. J. Fox, L. Chen, M. A. Khan and G. B. Richter-Addo, *Inorg. Chem.*, 1997, **36**, 6465-6467.
- L.-S. Wang, L. Chen, M. A. Khan and G. B. Richter-Addo, *Chem. Commun.*, 1996, 323-324.
- L. Chen, J. B. Fox, Jr., G.-B. Yi, M. A. Khan and G. B. Richter-Addo, *J. Porph. Phthalocyanines*, 2001, **5**, 702-707.
- R. S. Srivastava, M. A. Khan and K. M. Nicholas, *J. Am. Chem. Soc.*, 2005, **127**, 7278-7279.
- S. Wirth and I. P. Lorenz, *Z. Naturforsch. B*, 2012, **B67**, 532-542.
- R. G. Pearson, *J. Am. Chem. Soc.*, 1963, **85**, 3533-3539.
- R. S. Srivastava, N. R. Tarver and K. M. Nicholas, *J. Am. Chem. Soc.*, 2007, **129**, 15250-15258.
- M. S. Askari, B. Girard, M. Murugesu and X. Ottenwaelder, *Chem. Commun.*, 2011, **47**, 8055-8057.
- S. Hu, D. M. Thompson, P. O. Ikekwere, R. J. Barton, K. E. Johnson and B. E. Robertson, *Inorg. Chem.*, 1989, **28**, 4552-4554.
- N. C. Tomson, L. A. Labios, T. Weyhermuller, J. S. Figueroa and K. Wieghardt, *Inorg. Chem.*, 2011, **50**, 5763-5776.

36. L. Chen, M. A. Khan, G. B. Richter-Addo, V. G. Young, Jr. and D. R. Powell, *Inorg. Chem.*, 1998, **37**, 4689-4696.
37. D. Mansuy, J. C. Chottard and G. Chottard, *Eur. J. Biochem.*, 1977, **76**, 617-623.
38. D. Keilin and E. F. Hartree, *Nature*, 1943, **151**, 390-391.
39. J. M. Fukuto, J. F. Brady, J. N. Burstyn, R. B. VanAtta, J. S. Valentine and A. K. Cho, *Biochemistry*, 1986, **25**, 2714-2719.
40. D. Mansuy, P. Beaune, T. Cresteil, C. Bacot, J.-C. Chottard and P. Gans, *Eur. J. Biochem.*, 1978, **86**, 573-579.
41. J. Werringloer and R. W. Estabrook, *Arch. Biochem. Biophys.*, 1975, **167**, 270-286.
42. A. Renodon, J.-L. Boucher, C. Wu, R. Gachhui, M.-A. Sari, D. Mansuy and D. Stuehr, *Biochemistry*, 1998, **37**, 6367-6374.
43. R. Ricoux, J.-L. Boucher, D. Mansuy and J.-P. Mahy, *Biochem. Biophys. Res. Commun.*, 2000, **278**, 217-223.
44. R. Ricoux, E. Ludowska, F. Pezzotti and J.-P. Mahy, *Eur. J. Biochem.*, 2004, **271**, 1277-1283.
45. J. P. Mahy and D. Mansuy, *Biochemistry*, 1991, **30**, 4165-4172.
46. C. Rømming and H. J. Talberg, *Acta Chem. Scand.*, 1973, **27**, 2246-2248.
47. K. Lewinski, W. Nitek and P. Milart, *Acta Cryst.*, 1993, **C49**, 188-190.
48. H. J. Talberg, *Acta. Chem. Scand. A*, 1977, **31**, 743-751.
49. Y. Ling, C. Mills, R. Weber, L. Yang and Y. Zhang, *J. Am. Chem. Soc.*, 2010, **132**, 1583-1591.
50. M. Cameron, B. G. Gowenlock and G. Vasapollo, *J. Organomet. Chem.*, 1991, **325**, 325-333.
51. M. Cameron, B. G. Gowenlock and G. Vasapollo, *Polyhedron*, 1994, **13**, 1371-1377.
52. W. Lüttke, *Angew. Chem.*, 1958, **70**, 576-577.
53. M. Cameron, B. G. Gowenlock and G. Vasapollo, *J. Organomet. Chem.*, 1989, **378**, 493-496.
54. B. Knieriem, Ph.D. Dissertation, University of Göttingen, 1972.
55. C. J. Popp and R. O. Ragsdale, *Inorg. Chem.*, 1968, **7**, 1845-1848.
56. C. J. Popp and R. O. Ragsdale, *J. Chem. Soc. (A)*, 1970, 1822-1825.
57. K. Polat, M. L. Aksu and A. T. Pekel, *J. Appl. Electrochem.*, 2000, **30**, 733-736, and references therein.
58. W. R. Scheidt, in *The Porphyrin Handbook*, eds. K. M. Kadish, K. M. Smith and R. Guilard, Academic Press, New York, 2000, vol. 3, Chapter 16.
59. O. Q. Munro, P. S. Madlala, R. A. F. Warby, T. B. Seda and G. Hearne, *Inorg. Chem.*, 1999, **38**, 4724-4736.
60. N. Godbout, L. K. Sanders, R. Salzmann, R. H. Havlin, M. Wojdelski and E. Oldfield, *J. Am. Chem. Soc.*, 1999, **121**, 3829-3844.
61. D. H. Grant, *J. Chem. Educ.*, 1995, **72**, 39-40, and references therein.
62. R. L. Khade, A. L. Chandgude, R. Fasan and Y. Zhang, *ChemCatChem*, 2019, **11**, 3101-3108.
63. R. L. Khade, W. Fan, Y. Ling, L. Yang, E. Oldfield and Y. Zhang, *Angew. Chem. Int. Ed.*, 2014, **53**, 7574-7578.
64. R. L. Khade and Y. Zhang, *J. Am. Chem. Soc.*, 2015, **137**, 7560-7563.
65. R. L. Khade and Y. Zhang, *Chem. Eur. J.*, 2017, **23**, 17654-17658.
66. D. A. Vargas, R. L. Khade, Y. Zhang and R. Fasan, *Angew. Chem. Int. Ed.*, 2019, **58**, 10148-10152.
67. Y. Wei, A. Tinoco, V. Steck, R. Fasan and Y. Zhang, *J. Am. Chem. Soc.*, 2018, **140**, 1649-1662.
68. A. Tinoco, Y. Wei, J. P. Bacik, E. J. Moore, N. Ando, Y. Zhang and R. Fasan, *ACS Catalysis*, 2019, **9**, 1514-1524.
69. C. A. Reed, T. Mashiko, W. R. Scheidt, K. Spartalian and G. Lang, *J. Am. Chem. Soc.*, 1980, **102**, 2302-2306.
70. P. G. Debrunner, in *Iron Porphyrins*, ed. H. B. Gray and A. B. P. Lever, VCH Publishers, New York, 1989, pp. 139-234.
71. Y. Ling and Y. Zhang, *J. Am. Chem. Soc.*, 2009, **131**, 6386-6388.
72. A. D. Adler, F. R. Longo, J. D. Finarelli, J. Goldmacher, J. Assour and L. Korsakoff, *J. Org. Chem.*, 1967, **32**, 476.
73. A. D. Adler, F. R. Longo, F. Kampas and J. Kim, *J. Inorg. Nucl. Chem.*, 1970, **32**, 2443-2445.
74. E. T. Kintner and J. H. Dawson, *Inorg. Chem.*, 1991, **30**, 4892-4897.
75. K. Shelly, T. Bartczak and W. R. Scheidt, *Inorg. Chem.*, 1985, **24**, 4325-5330.
76. P. D. Caesar, *Org. Synth.*, 1963, **Coll. Vol. 4**, 695-696.
77. G. M. Bennett and E. V. Bell, *Org. Synth.*, 1943, **Coll. Vol. 2**, 223-225.
78. D. Samuel and I. Wassermann, *J. Labelled Comp.*, 1971, **7**, 355-356.
79. C. A. Reed, T. Mashiko, S. P. Bentley, M. E. Kastner, W. R. Scheidt, K. Spartalian and G. Lang, *J. Am. Chem. Soc.*, 1979, **101**, 2948-2958.
80. M. M. Maltempo and T. H. Moss, *Quart. Rev. Biophys.*, 1976, **9**, 181-215.
81. Bruker AXS Inc., Madison, WI, USA, 2016.
82. APEX2, Bruker-AXS, Madison, WI, USA, 2007.
83. SAINT, *Data Reduction: SAINT Software Reference Manual. Bruker-AXS, Madison, WI.*, 2007.
84. G. M. Sheldrick, *Acta Cryst.*, 2015, **C71**, 3-8.
85. L. Krause, R. Herbst-Irmer, G. M. Sheldrick and D. Stalke, *J. Appl. Cryst.*, 2015, **48**, 3-10.
86. A. L. Spek, *Acta Cryst.*, 2015, **C71**, 9-18.
87. M. J. Frisch, G. W. Trucks, H. B. Schlegel, G. E. Scuseria, M. A. Robb, J. R. Cheeseman, G. Scalmani, V. Barone, G. A. Petersson, H. Nakatsuji, X. Li, M. Caricato, A. V. Marenich, J. Bloino, B. G. Janesko, R. Gomperts, B. Mennucci, H. P. Hratchian, J. V. Ortiz, A. F. Izmaylov, J. L. Sonnenberg, Williams, F. Ding, F. Lipparini, F. Egidi, J. Goings, B. Peng, A. Petrone, T. Henderson, D. Ranasinghe, V. G. Zakrzewski, J. Gao, N. Rega, G. Zheng, W. Liang, M. Hada, M. T. Ehara, K., R. Fukuda, J. Hasegawa, M. Ishida, T. Nakajima, Y. Honda, O. Kitao, H. Nakai, T. Vreven, K. Throssell, J. A. Montgomery Jr., J. E. Peralta, F. Ogliaro, M. J. Bearpark, J. J. Heyd, E. N. Brothers, K. N. Kudin, V. N. Staroverov, T. A. Keith, R. Kobayashi, J. Normand, K. Raghavachari, A. P. Rendell, J. C. Burant, S. S. Iyengar, J. Tomasi, M. Cossi, J. M. Millam, M. Klene, C. Adamo, R. Cammi, J. W. Ochterski, R. L. Martin, K. Morokuma, O. Farkas, J. B. Foresman and D. J. Fox, *Gaussian-16 Rev. C.01*, Wallingford, CT, 2016.
88. J.-D. Chai and M. Head-Gordon, *Phys. Chem. Chem. Phys.*, 2008, **10**, 6615-6620.
89. P. J. Hay and W. R. Wadt, *J. Chem. Phys.*, 1985, **82**, 270-283.
90. Y. Minenkov, Å. Singstad, G. Occhipinti and V. R. Jensen, *Dalton Trans.*, 2012, **41**, 5526-5541.
91. E. G. Abucayon, R. L. Khade, D. R. Powell, Y. Zhang and G. B. Richter-Addo, *J. Am. Chem. Soc.*, 2016, **138**, 104-107.
92. E. G. Abucayon, R. L. Khade, D. R. Powell, M. J. Shaw, Y. Zhang and G. B. Richter-Addo, *Dalton Trans.* 2016, **45**, 18259-18266.
93. Y. Shi and Y. Zhang, *Angew. Chem. Int. Ed.*, 2018, **57**, 16654-16658.

